Muscle-Like Fatigue-Resistant Hydrogels by Mechanical Training

Shaoting Lin,[1*] Ji Liu,[1*] Xinyue Liu,[1] Xuanhe Zhao[1,2†]

[1]Department of Mechanical Engineering, Massachusetts Institute of Technology, Cambridge, MA 02139, USA

[2]Department of Civil and Environmental Engineering, Massachusetts Institute of Technology, Cambridge, MA 02139, USA

*Shaoting Lin and Ji Liu contributed equally to this work.

†To whom correspondence should be addressed. Email: zhaox@mit.edu

Keywords: Polyvinyl alcohol (PVA), Anti-fatigue-fracture, Freeze-thaw, Pre-stretch, 3D printing

One sentence summary: We propose a strategy of mechanical training to achieve the aligned nanofibrillar architectures of skeletal muscles in synthetic hydrogels, resulting in the combinational muscle-like properties for the first time.

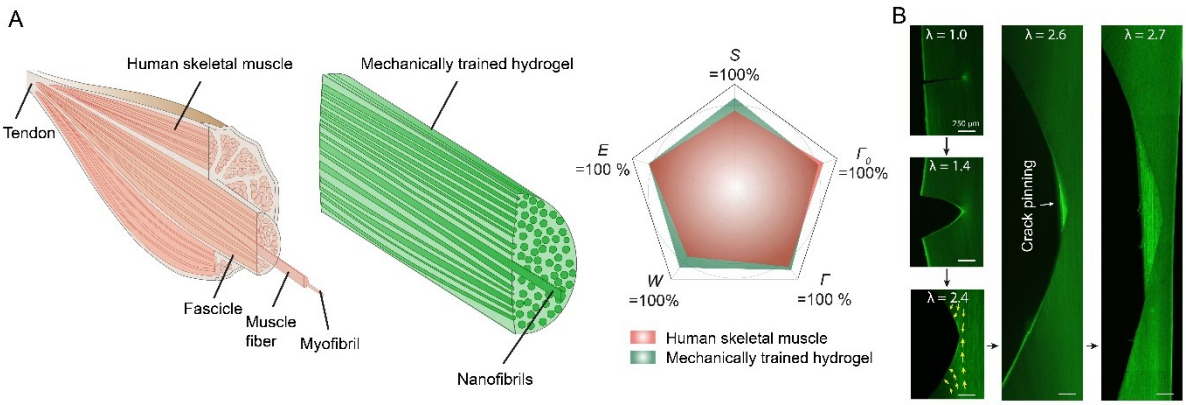

Author contributions

S.L., J.L., and X.Z. conceived the idea, designed the study and interpreted the results. S.L., J.L., and X.L. performed mechanical characterization and fatigue tests. S.L. performed DSC and TGA. J.L. performed SEM and AFM measurements. J.L. and S.L. performed confocal imaging and SAXS measurements. J.L. developed the set-up for *in situ* confocal imaging and *in situ* X-ray scattering measurements. J.L. developed the protocol for 3D printing PVA hydrogels with aligned nanofibrils. S.L., J.L., X.L., and X.Z. analyzed and interpreted the results. S.L., J.L., X.L., and X.Z. drafted the manuscript with inputs from all other authors. X.Z. supervised the study.

Muscle-Like Fatigue-Resistant Hydrogels by Mechanical Training

Abstract

Skeletal muscles possess the combinational properties of high fatigue resistances (1000 J/m^2), high strengths (1 MPa), low Young's moduli (100 kPa), and high water contents (70 − 80 wt%), which have not been achieved in synthetic hydrogels. The muscle-like properties are highly desirable for hydrogels' nascent applications in load-bearing artificial tissues and soft devices. Here, we propose a strategy of mechanical training to achieve the aligned nanofibrillar architectures of skeletal muscles in synthetic hydrogels, resulting in the combinational muscle-like properties for the first time. These properties are obtained through the training-induced alignment of nanofibrils, without additional chemical modifications or additives. *In situ* confocal microscopy of the hydrogels' fracturing processes reveals that the fatigue resistance results from the crack pinning by the aligned nanofibrils, which require much higher energy to fracture than the amorphous polymer chains. This strategy is particularly applicable for three-dimensionally printed microstructures of hydrogels, in which we can achieve isotropically fatigue-resistant, strong yet compliant properties.

Significance statement

The combinational muscle-like properties including high fatigue resistances, high strengths, superior compliances and high water contents are highly desirable for various applications of soft biomaterials such as hydrogels. These combinational properties, largely attributed to the aligned nanofibrils in natural muscles, have not been achieved in synthetic hydrogels. Here, we propose a strategy of mechanical training to impart hydrogels with an extremely high fatigue threshold (1250 J/m^2) and strength (5.2 MPa), while maintaining a high water content (84 wt%) and a low Young's modulus (200 kPa), reaching combinational muscle-like properties with aligned nanofibrillar architectures for the first time. We further achieve isotropically enhanced properties by three-dimensionally printing the hydrogels into microstructures.

\body

Main text

Biological load-bearing tissues such as skeletal muscles commonly show J-shaped stress-strain behaviors with low Young's moduli and high strengths on the order of 100 kPa and 1 MPa, respectively (1, 2). Moreover, despite their high water contents over 75 wt% (3), skeletal muscles can sustain a high stress of 1 MPa over 1 million cycles per year, with a fatigue resistance over 1000 J/m^2 (4). The combinational properties of skeletal muscles (i.e., high fatigue resistances, high strengths, superior compliances, and high water contents) are highly desirable for hydrogels' nascent applications in soft biological devices, such as load bearing artificial tissues (5), hydrogel bioelectronics (6-9), hydrogel optical fibers (10, 11), ingestible hydrogel devices (12), robust hydrogel coatings on medical devices (13-17), and hydrogel soft robots (18-20).

Although various molecular and macromolecular engineering approaches have replicated parts of biological muscles' characteristics, none of them can synergistically replicate all these attributes in one single material system (See *SI Appendix*,Table S1). For example, both strain-stiffening hydrogels (21, 22) and bottle brush polymer networks (1, 23) can mimic the J-shaped stress-strain behaviors, but their fracture toughnesses are still much lower than biological tissues, since no significant mechanical dissipation has been introduced in these materials for toughness enhancement. Although various tough hydrogels (24, 25) have been developed by incorporating various dissipation mechanisms, they are susceptible to fatigue fracture under repeated mechanical loads, since the resistance to fatigue crack propagation after prolonged repeated mechanical loads is the energy required to fracture a single layer of polymer chains, unaffected by the additional dissipation (26). Recently, introduction of well-controlled nanocrystalline domains (27) has shown to substantially increase a hydrogel's fatigue threshold (i.e., the minimal fracture energy at which crack propagation occurs under cyclic loads), but the

growth of nanocrystalline domains consumes interstitial amorphous polymer chains and therefore increases the Young's modulus and reduces the water content of the hydrogel.

Here, we propose a strategy to achieve the combinational muscle-like properties in synthetic hydrogels via mechanical training for the first time (Fig. 1*A*). Using freeze-thawed polyvinyl alcohol (PVA) hydrogel as a model material, we successfully mimic the aligned nanofibrillar architectures in skeletal muscles (Fig. 1*B*). The developed hydrogels by mechanical training can achieve an extremely high fatigue threshold (1250 J/m^2) and tensile strength (5.2 MPa), while maintaining a high water content (84 wt%) and low Young's modulus (200 kPa), reaching combinational muscle-level properties for the first time (28) (Fig. 1*C*). *In situ* confocal microscopy of the hydrogels' fracturing processes reveals that the fatigue-resistant (or anti-fatigue-fracture) mechanism for the hydrogels is the crack pinning by the aligned nanofibrils, which require much higher energy to fracture than the corresponding amorphous polymer chains. *In situ* X-ray scattering of the hydrogels under elongation further reveals that the low Young's moduli of the hydrogels are attributed to the stretching of polymer chains, orientation of nanocrystalline domains and sliding of aligned nanofibrils under moderate stretches.

Results

Design of muscle-like hydrogels. Figure 1*A* schematically illustrates our strategy to design synthetic hydrogels with combinational properties comparable to skeletal muscles. The strategy first involves growing compliant nanofibrils in PVA hydrogels by forming two separated phases (29): i). high concentration of polymer chains in the form of nanofibrils cross-linked by nanocrystalline domains, and ii). low concentration of amorphous polymer chains. PVA polymer chains possess abundant hydroxyl side groups, which can readily form intra-/inter-chain hydrogen bonding. Upon exposure to a low temperature below freezing temperature (i.e., -20 °C), the water freezes and forms ice crystals that can expel PVA chains to form regions of high polymer concentrations. As the PVA chains come into close contact with each other, nanocrystalline domains nucleate with the formation of hydrogen bonds (29-31). These

interactions (i.e., hydrogen bonding) remain intact in the subsequent thawing process, leading to a physically cross-linked network of nanofibrils. The dendritic growth of ice crystals further leads to a random distribution of these nanofibrils (32).

To form the aligned nanofibrillar structures, the pristine freeze-thawed hydrogels with randomly-distributed nanofibrils are exposed to repeated pre-stretches in a water bath as mechanical training, similar to the exercise of skeletal muscles. Under repeated exercise, skeletal muscles get strengthened by self-growing, accompanied by the disruption of the nanofibrillar structures in skeletal muscle and growth of new muscle nanofibrils (33). Similarly, repeated pre-stretches applied on the hydrogels with randomly-distributed nanofibrils are accompanied by the disruption of randomly-oriented nanocrystalline domains, followed by gradual alignment of nanofibrils with newly-formed aligned nanocrystalline domains (34). One merit of our training strategy is that it does not require any extra supply of building blocks (i.e., monomers) during the mechanical training (35).

Random and aligned nanofibrillar structures. We first use the confocal laser scanning microscopy to visualize the nanofibrils in the pristine freeze-thawed PVA hydrogel. Fluorochrome is conjugated to the PVA macromolecules by immersing the freeze-thawed hydrogels in a reactive dye solution (36) (See *SI Appendix*, Fig. S1). With the conjugated fluorochromes, the PVA-rich phases are visible in green in the form of randomly-distributed nanofibrils (Fig. 2*A*), while regions with relatively low concentrations of PVA polymers (i.e., water-rich phase between adjacent nanofibrils) are dark. As a control, the chemically cross-linked PVA hydrogel shows green luminance with uniform brightness, indicating the uniform distribution of PVA amorphous chains (See *SI Appendix*, Fig. S2).

We next show that the freeze-thawed PVA hydrogel can form aligned nanofibrillar structures by repeated pre-stretches in a water bath (Fig. 2*A* and *SI Appendix*, Fig. S3*A*). The confocal images of the pre-stretched PVA hydrogel in Fig. 2*A* and *SI Appendix*, Fig. S4 confirm that the randomly-distributed nanofibrils gradually reorient and align towards the direction of the applied pre-stretches. It is noted that once the first cycle of pre-stretch is relaxed, the aligned nanofibrils mostly recover their previous random distribution elastically (See *SI Appendix*, Fig.

S4). As the cycle number increases, plastic deformation accumulates in the hydrogel, which gradually elongates along the pre-stretched direction, and finally preserves the alignment (See *SI Appendix*, Fig. S5). The alignment of nanofibrils reaches a steady state after sufficient cycles of pre-stretches (i.e., 1000 cycles of pre-stretches of 4.6). The alignment of the nanofibrils in the pre-stretched PVA hydrogels is also validated through scanning electron microscopy (SEM) images (Fig. 2*C*) and atomic force microscopy (AFM) phase images (Fig. 2*D*). Small angle X-ray scanning (SAXS) patterns (Fig. 2*B*) further reveal that the nanocrystalline domains in nanofibrils have been reoriented during the pre-stretches. In addition, the measured diameters of the nanofibrils range from ~200 nm to ~1 μm (See *SI Appendix*, Fig. S6 and Fig. 2 *A* and *C*).

Existing approaches to introduce ordered nanocrystalline domains and aligned structures in hydrogels include cold-drawing (37), pre-stretching in air (38), and constrained air-drying (39), which fail to retain their original high water contents, due to the formation of additional excessive nanocrystalline domains. By contrast, the pre-stretched PVA hydrogel obtained from our strategy can still maintain a high water content of 84 wt% (Fig. 3*C*), close to the pristine freeze-thawed PVA samples (88 wt%). The differential scanning calorimetry (DSC) results further show that the crystallinity in the swollen state of the pre-stretched PVA hydrogel is only 2.8 wt% (See *SI Appendix*, Fig. S8), slightly higher than the pristine freeze-thawed PVA hydrogel (1.8 wt%) (Fig. 3*C*). The slightly increased crystallinity could be attributed to the newly-formed nanocrystalline domains during the nanofibrillar alignments under cyclic pre-stretches (40). Both high water content and low crystallinity in our pre-stretched PVA hydrogel indicate that our strategy could substantially suppress the undesirable excessive crystallization while maintaining water contents and compliances of the hydrogels.

Combinational muscle-like properties. We further demonstrate the combinational muscle-like mechanical properties in the pre-stretched PVA hydrogel (Fig. 3). At small stretches, the pre-stretched PVA hydrogel demonstrates a low Young's modulus along directions both parallel (210 kPa) and perpendicular (140 kPa) to the aligned nanofibrils, similar to the pristine freeze-thawed PVA hydrogels (100 kPa) (Fig. 3 *A* and *D*). At high stretches, the

pre-stretched PVA hydrogel stiffens drastically parallel to the aligned nanofibrils, exhibiting a J-shaped stress versus stretch curve, similar to that of skeletal muscles (1). In addition, the pre-stretched PVA hydrogel shows an extremely high ultimate nominal tensile strength of 5.2 MPa parallel to the aligned nanofibrils, which is 4.3 times of the pristine freeze-thawed hydrogel's strength (1.2 MPa) and 26 times of the chemically cross-linked hydrogel's strength (0.2 MPa) (Fig. 3 *A* and *D*). The ultimate nominal tensile strength of the pre-stretched PVA hydrogel perpendicular to nanofibrils is measured to be 1.1 MPa, close to the value of the pristine freeze-thawed hydrogel (i.e., 1.2 MPa). The pre-stretched PVA hydrogel also shows high resilience with negligible hysteresis when stretched along the aligned nanofibrils (See *SI Appendix*, Fig. S9). The fatigue threshold of the pre-stretched PVA hydrogel measured along the aligned nanofibrils reaches a record-high value of 1,250 J/m^2 (Fig. 3*B*), orders of magnitude higher than those of existing tough hydrogels (10~100 J/m^2) (41-43). To validate the high fatigue threshold of the pre-stretched PVA hydrogels parallel to the aligned nanofibrils, we also apply cyclic loads on a single-notch tensile specimen with the energy release rate of 1250 J/m^2 and observe no crack extension over 30,000 cycles (See *SI Appendix*, Fig. S10). By contrast, the fatigue threshold perpendicular to the aligned nanofibrils is 233 J/m^2, which is on the same order as that of the pristine freeze-thawed PVA hydrogel (i.e., 310 J/m^2, *SI Appendix*, Fig. S10), but still much larger than that of the chemically cross-linked PVA hydrogel (i.e., 10 J/m^2, *SI Appendix*, Fig. S11).

To compare our results with existing hydrogels and biological tissues, we summarize the nominal tensile strengths, Young's moduli, fatigue thresholds, and water contents of various tough hydrogels (24, 25, 27, 39, 44-48) and biological tissues (1) in Fig. 3*E* and 3*F*. The strength-modulus ratios *S*/*E* of existing tough hydrogels such as PAAm-alginate (24), PVA-PAAm (47), dry annealed PVA (27), freeze-thawed PVA (49), polyampholyte hydrogels (46), fiber reinforced hydrogel composites (44, 50), wood hydrogels (45), and constrained air-drying hydrogels (39) are in the range of 0.1 to 10 (Fig. 3*E*). Remarkably, the strength-modulus ratio *S*/*E* of the pre-stretched PVA hydrogel is as high as 50, since the high strength of the pre-stretched PVA hydrogel is accompanied by its low Young's modulus.

In addition to the challenge in designing synthetic hydrogels with superior compliances and high strengths, the combinational properties of high fatigue threshold and high water content have not been achieved in existing hydrogels (Fig. 3*F*). By following our strategy, the fatigue threshold of the pre-stretched PVA hydrogel can achieve a high value of 1,250 J/m^2 along with a high water content of 84 wt%, outperforming existing hydrogels and biological tissues.

Mechanisms for superior compliances. *In situ* small angle X-ray scattering (SAXS) measurements offer insights into the mechanism for the superior compliance of the pre-stretched PVA hydrogel at small deformations (Fig. 4*A*). The nanocrystalline morphology in the pre-stretched PVA hydrogel (in the swollen state) is investigated by SAXS analysis at the applied stretch of 1, 1.4, 1.8, and 2.2. As shown in Fig. 4 *B* and *D*, the average distance between neighboring nanocrystalline domains parallel to aligned nanofibrils $L\parallel$ (i.e., $\theta = 0°$) for the pre-stretched PVA hydrogel at undeformed state (i.e., $\lambda = 1$) is estimated to be 13.2 nm. As the applied stretch increases to 2.2, the average distance between neighboring nanocrystalline domains increases to 15.5 nm (Fig. 4*D*), which indicates the stretching of interstitial amorphous chains between the adjacent nanocrystalline domains in the nanofibrils. Since the stretch of interstitial amorphous chains (e.g., 15.5 nm/13.2 nm) is much lower than the corresponding applied stretch (e.g., 2.2), sliding between nanofibrils may also occur during stretching. In comparison, the scattering curves show negligible difference at different stretches perpendicular to the aligned nanofibrils $L\perp$ (i.e., $\theta = 90°$) (Fig. 4*C*), which implies the average distance between neighboring nanocrystalline domains perpendicular to the aligned nanofibrils $L\perp$ (i.e., $\theta = 90°$) remains constant with negligible lateral contraction as the stretch increases.

We further plot the scattering intensity I versus direction θ to quantify the degree of orientation of nanocrystalline domains during stretching (Fig. 4*E*). At the undeformed state (i.e., $\lambda = 1$), there are peaks along the pre-stretched direction (i.e., $\theta = 0°$), implying that the orientation of nanocrystalline domains along the pre-stretched direction exists in the

undeformed sample. As the applied stretch increases, the peaks along the pre-stretched direction (i.e., $\theta = 0°$) become more pronounced, indicating that the applied stretch can drive additional orientation of nanocrystalline domains. Overall, the stretch of interstitial amorphous chains, orientation of nanocrystalline domains and sliding between nanofibrils account for the superior compliance of the pre-stretched PVA hydrogel at moderate deformations along the aligned nanofibrils.

Furthermore, the high compliances of the pristine freeze-thawed PVA hydrogel and the pre-stretched PVA hydrogel stretched perpendicularly to the aligned nanofibrils can be attributed to the orientation of randomly-distributed nanofibrils and the stretching of amorphous polymer chains between adjacent nanofibrils, respectively.

Mechanisms for high fatigue thresholds. *In situ* confocal laser scanning microscopy further explains the mechanism for the high fatigue threshold of the pre-stretched PVA hydrogel. As shown in Fig. 5 *A* and *B*, the aligned nanofibrils are perpendicular to the crack path and pin the crack due to the high strength of the nanofibrils. There is no observable crack propagation at the applied stretch of 2.4. As the applied stretch further increases to 2.6, the nanofibrils at the crack tip are pulled out from the hydrogel but still bridge the crack tip. As the crack propagates, the rupture of the nanofibrils requires a much higher energy per unit area than fracturing the corresponding amorphous polymer chains, giving rise to a much higher fatigue threshold (1250 J/m^2) than that of the amorphous polymer networks (10 J/m^2). Notably, the crack pinned by the aligned nanofibrils does not branch or tilt under high static and cyclic loads (e.g., Fig. 5B and *SI Appendix*, Fig. S10), assuring the hydrogel's high fatigue threshold. By contrast, crack branching and tilting has been observed in hydrogels reinforced by microscale phase separation (51) and in elastomers reinforced by macroscale fibers (52). It will be interesting to study the effects of the reinforcements across different length scales in future.

When the crack is parallel to the aligned nanofibrils, the crack begins to propagate in between neighboring nanofibrils at the applied stretch of 1.5, fracturing interstitial amorphous

chains between the adjacent nanofibrils (Fig. 5 *C* and *D*). Similarly, in freeze-thawed PVA hydrogel, the initially randomly-oriented nanofibrils gradually align parallel to the crack contour with the increase of the applied stretch, followed by fracturing interstitial amorphous chains (Fig. 5 *E* and *F*). In addition, due to the very long amorphous chains between the adjacent nanofibrils (26), the fatigue thresholds of the pristine freeze-thawed PVA hydrogel and the pre-stretched PVA hydrogel with a crack along the aligned nanofibrils are still moderately high (310 J/m^2 and 233 J/m^2, respectively).

3D printing of isotropically fatigue-resistant, strong yet compliant micromeshes. The aligned nanofibrils give notably anisotropic mechanical behaviors of the pre-stretched PVA hydrogel, similar to that of skeletal muscles. However, for many applications, it is desirable to achieve isotropically muscle-level properties. Here, we propose to 3D print microstructures of hydrogels and mechanically train the structures to achieve fatigue-resistant, strong yet compliant properties in both in-plane directions. To demonstrate such potential, we develop PVA ink and print microstructures with square meshes as shown in *SI Appendix*, Fig. S12*A*. The confocal image of the 3D-printed PVA filaments with a diameter of 750 μm shows random distributions of nanofibrils before mechanical training (Fig. 6*A* and *SI Appendix*, Fig. S12*B*). During mechanical training, the printed microstructure undergoes biaxial cyclic pre-stretches in a water bath (i.e., pre-stretch of 3.5 over 1000 cycles). The trained PVA filaments with a reduced diameter of 500 μm (See *SI Appendix*, Fig. S12*B*) show pronounced alignments of nanofibrils along the filaments from the confocal images and the SAXS patterns (Fig. 6*B*). We further measure the effective nominal stress (i.e. the force divided by the cross-section area of the microstructure) versus stretch of the PVA mesh before and after training. The effective Young's moduli of the pre-stretched mesh along both in-plane directions are measured to be 70 kPa, which is slightly higher than that of the pristine mesh (Fig. 6*D*). The effective nominal strengths of the pre-stretched mesh along both in-plane directions are measured to be 500 kPa, which is 1.5 times higher than that of the pristine mesh (Fig. 6*E*). We further apply cyclic loads

on both meshes before and after training with a notch (Fig. 6*C*), evaluating their effective fatigue thresholds (i.e., the minimal energy release rate at which crack propagation occurs in the mesh under cyclic loads). The effective fatigue threshold of the pre-stretched mesh after training reaches 1000 J/m^2 in both in-plane directions, 2 times higher than that of the pristine mesh (Fig. 6*F*).

Conclusions

The classical Lake-Thomas model predicts that the fatigue threshold of a polymer network is the energy required to fracture a single layer of amorphous polymer chains, on the order of 1-100 Jm^{-2} (26). We have proposed that the design principle for fatigue-resistant (or anti-fatigue-fracture) hydrogels is to make the fatigue crack encounter and fracture objects requiring energies per unit area much higher than that for fracturing a single layer of amorphous polymer chains (27). We have shown that high densities of nanocrystalline domains in hydrogels can act as the high-energy phase to effectively pin fatigue cracks and greatly enhance the fatigue thresholds of nanocrystalline hydrogels up to 1000 J/m^2, exceeding the Lake-Thomas limit (27). However, the nanocrystalline domains also significantly increase the Young's moduli of the hydrogels, due to nanocrystalline domains' high rigidity over 1 GPa (27).

While a much higher energy is also required to fracture nanofibrils than the corresponding amorphous polymer chains, the rigidity of nanofibrils under moderate stretches can be designed to be relatively low (53). In this paper, we further establish that aligning these nanofibrils in hydrogels by mechanical training can empower the integration of muscle-like performances, i.e., high fatigue thresholds (1250 J/m^2), high strengths (5.2 MPa), low Young's moduli (200 kPa) and high water contents (84 wt%), into one single hydrogel material. In addition, we achieve isotropically enhanced properties by 3D printing the hydrogel into microstructures followed by mechanical training. The capability of making strong, fatigue-resistant yet soft hydrogels can enable various biomedical applications that interact with the

human body for long-lasting performances. This work also opens a new avenue to mechanically engineer alignments of nanofibrils and orientations of nanocrystalline domains in hydrogels.

Methods

All details associated with sample preparations, *in situ* confocal imaging, *in situ* X-ray scattering, SEM imaging, AFM phase imaging, Mechanical characterization, Measurement of water contents and crystallinities, and 3D printing of PVA meshes appear in SI Appendix.

Material preparation. The freeze-thawed PVA was fabricated by freezing 10 wt% PVA solution at -20 °C for 8 hours and thawing at 25 °C for 3 hours with five repeated cycles. The mechanically trained PVA hydrogel was fabricated by cyclically pre-stretching the freeze-thawed hydrogel in a water bath using mechanical stretcher (Cellscale, Canada). The sufficiently aligned nanofibrils were achieved by applying the maximum applied stretch of 4.6 for 1000 cycles at a stretch rate of 0.3 /s.

Confocal imaging of PVA hydrogels. To visualize the microstructures of the PVA hydrogels, a fluorescent dye (i.e., 5-([4,6-dichlorotriazin-2-yl]amino)fluorescein hydrochloride (5-DTAF)) was used to label the PVA side groups. Specifically, PVA hydrogel samples were first immersed in a large volume of sodium bicarbonate solution (0.1 M, pH 9.0) for 12 hours to equilibrate the pH within the samples. 5 mg of 5-DTAF dissolved in 1.0 mL of anhydrous dimethyl sulfoxide (DMSO) was further immersed into 100 ml of sodium bicarbonate solution (0.1 M, pH 9.0) to form a reactive dye solution. The pH-equilibrated PVA samples were immersed in the dye solution for 12 hours at 4 °C in the dark to form conjugated fluorochromes. Finally, the hydrogel samples were rinsed several times with deionized water to wash away the non-conjugated dyes, prior to fluorescence imaging.

Mechanical characterization. All the mechanical tests were performed using a U-stretch testing device (Cellscale, Canada) at a deformation rate of 0.3 /s. Young's Modulus, strength,

and fatigue threshold were measured in a water bath to prevent dehydration, following the method established in the paper (27).

3D printing of PVA hydrogels. The prepared PVA inks were stored in the 5 mL syringe barrels, which fit nozzles with diameters of 400 μm (EFD Nordson). To achieve stable and optimal printing, we chose 50 kPa of air pressure (Ultimus V, Nordson EFD) as the printing pressure, and 15 wt% PVA (146 kDa, 99% hydrolysis ratio) as the ink. After deposition, the printed samples were treated by five cycles of freezing (-20 °C for 8 hours) and thawing (20 °C for 3 hours) to achieve the final PVA hydrogel meshes.

Acknowledgments

The authors acknowledge J. Zhou at MIT for helping on preparing supercritical drying samples using supercritical dryer (Automegasamdri Series C, Tousimis) at Prof. E.N. Wang lab at MIT, and M. Z. Wyttenbach at MIT for the proofreading. This work was supported by National Science Foundation (CMMI-1661627), Office of Naval Research (N00014-17-1-2920), and U. S. Army Research Office through the Institute for Soldier Nanotechnologies at MIT (W911NF-13-D-0001).

References

1. Vatankhah-Varnosfaderani M*, et al.* (2018) Chameleon-like elastomers with molecularly encoded strain-adaptive stiffening and coloration. *Science* 359:1509-1513.
2. Gillies AR & Lieber RL (2011) Structure and function of the skeletal muscle extracellular matrix. *Muscle Nerve* 44:318-331.
3. Tavichakorntrakool R*, et al.* (2007) K+, Na+, Mg2+, Ca2+, and water contents in human skeletal muscle: correlations among these monovalent and divalent cations and their alterations in K+-depleted subjects. *Transl Res* 150:357-366.
4. Taylor D, O'Mara N, Ryan E, Takaza M, & Simms C (2012) The fracture toughness of soft tissues. *J Mech Behav Biomed Mater* 6:139-147.
5. Baker MI, Walsh SP, Schwartz Z, & Boyan BD (2012) A review of polyvinyl alcohol and its uses in cartilage and orthopedic applications. *J Biomed Mater Res B Appl Biomater* 100:1451-1457.
6. Zhao S*, et al.* (2018) Programmable Hydrogel Ionic Circuits for Biologically Matched Electronic Interfaces. *Adv Mat* 30:1800598.
7. Liu Y*, et al.* (2019) Soft and elastic hydrogel-based microelectronics for localized low-voltage neuromodulation. *Nat Biomed Eng* 3:58.

8. Lu B, *et al.* (2019) Pure PEDOT: PSS hydrogels. *Nat Commun* 10:1043.
9. Yuk H, Lu B, & Zhao X (2019) Hydrogel bioelectronics. *Chem Soc Rev* 48:1642-1667.
10. Guo J, *et al.* (2016) Highly stretchable, strain sensing hydrogel optical fibers. *Adv Mater* 28:10244-10249.
11. Choi M, Humar M, Kim S, & Yun SH (2015) Step-index optical fiber made of biocompatible hydrogels. *Adv Mater* 27:4081-4086.
12. Liu X, *et al.* (2019) Ingestible hydrogel device. *Nat Commun* 10:493.
13. Parada GA, Yuk H, Liu X, Hsieh AJ, & Zhao X (2017) Impermeable robust hydrogels via hybrid lamination. *Adv Healthc Mater* 6:1700520.
14. Yuk H, Zhang T, Lin S, Parada GA, & Zhao X (2016) Tough bonding of hydrogels to diverse non-porous surfaces. *Nat Mater* 15:190.
15. Yuk H, Zhang T, Parada GA, Liu X, & Zhao X (2016) Skin-inspired hydrogel–elastomer hybrids with robust interfaces and functional microstructures. *Nat Commun* 7:12028.
16. Takahashi R, *et al.* (2018) Tough Particle-Based Double Network Hydrogels for Functional Solid Surface Coatings. *Adv Mater Interfaces* 5:1801018.
17. Yu Y, *et al.* (2018) Multifunctional "Hydrogel Skins" on Diverse Polymers with Arbitrary Shapes. *Adv Mater* 31:1807101.
18. Yuk H, *et al.* (2017) Hydraulic hydrogel actuators and robots optically and sonically camouflaged in water. *Nat Commun* 8:14230.
19. Kim Y, Yuk H, Zhao R, Chester SA, & Zhao X (2018) Printing ferromagnetic domains for untethered fast-transforming soft materials. *Nature* 558:274.
20. Chin SY, *et al.* (2017) Additive manufacturing of hydrogel-based materials for next-generation implantable medical devices. *Sci Robot* 2:eaah6451.
21. Jaspers M, *et al.* (2014) Ultra-responsive soft matter from strain-stiffening hydrogels. *Nat Commun* 5:5808.
22. Kouwer PH, *et al.* (2013) Responsive biomimetic networks from polyisocyanopeptide hydrogels. *Nature* 493:651.
23. Vatankhah-Varnosfaderani M, *et al.* (2017) Mimicking biological stress–strain behaviour with synthetic elastomers. *Nature* 549:497.
24. Sun J-Y, *et al.* (2012) Highly stretchable and tough hydrogels. *Nature* 489:133.
25. Gong JP, Katsuyama Y, Kurokawa T, & Osada Y (2003) Double-network hydrogels with extremely high mechanical strength. *Adv Mater* 15:1155-1158.
26. Lake G & Thomas A (1967) The strength of highly elastic materials. *Proc R Soc Lond A* 300:108-119.
27. Lin S, *et al.* (2019) Anti-fatigue-fracture hydrogels. *Sci Adv* 5:eaau8528.
28. Kinloch AJ (2013) *Fracture behaviour of polymers* (Springer Science & Business Media).
29. Hassan CM & Peppas NA (2000) Structure and morphology of freeze/thawed PVA hydrogels. *Macromolecules* 33:2472-2479.
30. Peppas NA (1975) Turbidimetric studies of aqueous poly (vinyl alcohol) solutions. *Macromol Chem Phys* 176:3433-3440.
31. Holloway JL, Lowman AM, & Palmese GR (2013) The role of crystallization and phase separation in the formation of physically cross-linked PVA hydrogels. *Soft Matter* 9:826-833.
32. Willcox PJ, *et al.* (1999) Microstructure of poly (vinyl alcohol) hydrogels produced by freeze/thaw cycling. *J Polym Sci B* 37:3438-3454.
33. Schoenfeld BJ (2010) The mechanisms of muscle hypertrophy and their application to resistance training. *J Strength Cond Res* 24:2857-2872.
34. Toki S, Fujimaki T, & Okuyama M (2000) Strain-induced crystallization of natural rubber as detected real-time by wide-angle X-ray diffraction technique. *Polymer* 41:5423-5429.
35. Matsuda T, Kawakami R, Namba R, Nakajima T, & Gong JP (2019) Mechanoresponsive self-growing hydrogels inspired by muscle training. *Science* 363:504-508.
36. Fergg F, Keil F, & Quader H (2001) Investigations of the microscopic structure of poly (vinyl alcohol) hydrogels by confocal laser scanning microscopy. *Colloid Polym Sci* 279:61-67.
37. Sehaqui H, *et al.* (2012) Cellulose nanofiber orientation in nanopaper and nanocomposites by cold drawing. *ACS Appl Mater Interfaces* 4:1043-1049.

38. Fukumori T & Nakaoki T (2015) High strength poly (vinyl alcohol) films obtained by drying and then stretching freeze/thaw cycled gel. *J Appl Polym Sci* 132:41318.
39. Mredha MTI*, et al.* (2018) A Facile Method to Fabricate Anisotropic Hydrogels with Perfectly Aligned Hierarchical Fibrous Structures. *Adv Mater* 30:1704937.
40. Zhang Q*, et al.* (2018) Stretch-induced structural evolution of poly (vinyl alcohol) film in water at different temperatures: An in-situ synchrotron radiation small-and wide-angle X-ray scattering study. *Polymer* 142:233-243.
41. Bai R*, et al.* (2017) Fatigue fracture of tough hydrogels. *Extreme Mech Lett* 15:91-96.
42. Zhang W*, et al.* (2017) Fatigue of double-network hydrogels. *Eng Fract Mech* 187:74-93.
43. Bai R, Yang J, & Suo Z (2019) Fatigue of hydrogels. *Eur J Mech A-Solid* 74:337-370.
44. Haraguchi K & Takehisa T (2002) Nanocomposite hydrogels: a unique organic–inorganic network structure with extraordinary mechanical, optical, and swelling/de-swelling properties. *Adv Mater* 14:1120-1124.
45. Kong W*, et al.* (2018) Muscle-Inspired Highly Anisotropic, Strong, Ion-Conductive Hydrogels. *Adv Mater* 30:1801934.
46. Sun TL*, et al.* (2013) Physical hydrogels composed of polyampholytes demonstrate high toughness and viscoelasticity. *Nat Mater* 12:932.
47. Li J, Suo Z, & Vlassak JJ (2014) Stiff, strong, and tough hydrogels with good chemical stability. *J Mater Chem B* 2:6708-6713.
48. Lin S, Zhou Y, & Zhao X (2014) Designing extremely resilient and tough hydrogels via delayed dissipation. *Extreme Mech Lett* 1:70-75.
49. Stauffer SR & Peppast NA (1992) Poly (vinyl alcohol) hydrogels prepared by freezing-thawing cyclic processing. *Polymer* 33:3932-3936.
50. Lin S*, et al.* (2014) Design of stiff, tough and stretchy hydrogel composites via nanoscale hybrid crosslinking and macroscale fiber reinforcement. *Soft matter* 10:7519-7527.
51. Bai R, Yang J, Morelle XP, & Suo Z (2019) Flaw-Insensitive Hydrogels under Static and Cyclic Loads. *Macromol Rapid Commun* 2019:1800883.
52. Wang Z*, et al.* (2019) Stretchable materials of high toughness and low hysteresis. *Proc Natl Acad Sci USA* 116:5967-5972.
53. Ling S, Kaplan DL, & Buehler MJ (2018) Nanofibrils in nature and materials engineering. *Nat Rev Mater* 3:18016.

Figure legends

Fig. 1. Design of muscle-like hydrogels. *(A)* Schematic illustration of the microstructure of a PVA hydrogel with randomly-oriented nanofibrils before mechanical training and a PVA hydrogel with aligned nanofibrils after mechanical training (i.e., cyclic pre-stretches). *(B)* Similar aligned nanofibrillar architectures of human skeletal muscles and mechanically trained hydrogels. *(C)* Comparison of combinational properties of human skeletal muscle and mechanically trained hydrogel.

Fig. 2. Microstructures of PVA hydrogels before and after mechanical training. *(A)* Confocal images and corresponding histograms of a hydrogel with randomly-oriented nanofibrils before training (i.e., freeze-thawed PVA) and a hydrogel with aligned nanofibrils after training (i.e., pre-stretched PVA). P in the histograms represents the probability of nanofibrils at each aligned direction θ. *(B)* SAXS patterns and corresponding scattering intensity I vs. Azimuthal angle θ curve of a hydrogel with randomly-oriented nanofibrils before training (i.e., freeze-thawed PVA), and hydrogel with aligned nanofibrils after training (i.e., pre-stretched PVA). a.u., arbitrary units. *(C)* SEM images of a hydrogel with randomly-oriented nanofibrils before training (i.e., freeze-thawed PVA) and a hydrogel with aligned nanofibrils after training (i.e., pre-stretched PVA). *(D)* AFM phase images of a hydrogel with randomly-oriented nanofibrils before training (i.e., freeze-thawed PVA) and a hydrogel with aligned nanofibrils after training (i.e., pre-stretched PVA). Scale bars are 50 μm in *(A)*, 20 μm for left image in *(C)*, 10 μm for right image in *(C)*, and 100 nm in *(D)*.

Fig. 3. Mechanical properties of PVA hydrogels before and after mechanical training. *(A)* Nominal stress versus stretch curves of chemically cross-linked (Ch), freeze-thawed (FT), and pre-stretched PVA hydrogels parallel to (PFT //) and perpendicular to (PFT ⊥) nanofibrils. The X mark indicates the point of fracture. *(B)* Crack extension per cycle d*c*/d*N* versus applied energy release rate *G* of pre-stretched PVA hydrogels parallel to (PFT //) and perpendicular to (PFT ⊥) nanofibrils. *(C)* Summarized water contents and crystallinities in the swollen state of chemically cross-linked PVA (Ch), freeze-thawed PVA (FT), and pre-stretched PVA (PFT). *(D)* Summarized Young's moduli *E*, ultimate nominal tensile strengths *S*, and fatigue thresholds Γ_0 of chemically cross-linked (Ch), freeze-thawed (FT) and pre-stretched PVA hydrogels parallel to (PFT //) and perpendicular to (PFT ⊥) nanofibrils. *(E)* Comparison chart in the plot of nominal tensile strength and Young's modulus among tough hydrogels (e.g., PAAm-alginate (24), polyampholyte (46), freeze-thawed PVA (27), dry-annealed PVA (27), PVA-PAAm (47), and hydrogel composites (50)), biological tissues (e.g., skeletal muscle (1, 2)) and trained hydrogel (i.e., pre-stretched PVA). The dashed lines denote the linear relation between strength and modulus with strength-modulus ratio *S*/*E* of 0.1, 1, and 10. *(F)* Comparison chart in the plot of fatigue thresholds and water contents among tough hydrogels (43) (e.g., PAAm-alginate, PAAm-PAMPS, freeze-thawed PVA) and nanocrystalline hydrogels (e.g., dry-annealed PVA) (27), biological tissues (e.g., skeletal muscle), and trained hydrogel (i.e., pre-stretched PVA). Data in *(C)* and *(D)* are means ± SD, n = 3.

Fig. 4. Mechanisms for high compliances of pre-stretched PVA hydrogels with aligned nanofibrils. *(A)* Nominal stress versus stretch curve of pre-stretched PVA hydrogel with aligned nanofibrils and corresponding SAXS pattern at the stretch of 1, 1.4, 1.8, and 2.2. *(B)* The corrected scattering intensity Iq^2 versus vector q parallel to nanofibrils (i.e., $\theta = 0°$) of pre-stretched PVA hydrogel at the stretch of 1, 1.4, 1.8, and 2.2. *(C)* The corrected scattering intensity Iq^2 versus vector q perpendicular to nanofibrils (i.e., $\theta = 90°$) of pre-stretched PVA hydrogel at the stretch of 1, 1.4, 1.8, and 2.2. *(D)* Calculated average distance between adjacent nanocrystalline domains of pre-stretched PVA hydrogel parallel to nanofibrils $L_{/\!/}$ (i.e., $\theta = 0°$) and perpendicular to nanofibrils $L_{\perp}$ (i.e., $\theta = 90°$) at the stretch of 1, 1.4, 1.8, and 2.2. *(E)* The measured scattering intensity I vs. Azimuthal angle θ curves of pre-stretched PVA hydrogel at the stretch of 1, 1.4, 1.8, and 2.2. a.u., arbitrary units. Data in *(D)* are means ± SD, n = 3. The dashed red lines in the inset scattering pattern in *(B)* and *(C)* indicate the direction parallel to nanofibrils and perpendicular to nanofibrils, respectively.

Fig. 5. Mechanisms for high fatigue thresholds of pre-stretched PVA hydrogels with aligned nanofibrils. Schematic illustration of nanofibril morphology in *(A)* notched pre-stretched PVA hydrogel where crack is perpendicular to the longitudinal direction of nanofibrils, *(C)* notched pre-stretched PVA hydrogel where crack is parallel to the longitudinal direction of nanofibrils, and *(E)* freeze-thawed PVA hydrogel. Corresponding confocal images of notched samples under different stretches for *(B)* pre-stretched PVA hydrogel where crack is perpendicular to the longitudinal direction of nanofibrils, *(D)* pre-stretched PVA hydrogel where crack is parallel to the longitudinal direction of nanofibrils, and *(F)* freeze-thawed PVA hydrogel. The yellow arrows in confocal images indicate the direction of aligned nanofibrils around crack tip. Scale bars are 250 μm in *(B)*, 100 μm in *(D)*, and 250 μm in *(F)*.

Fig. 6. Isotropically fatigue-resistant, strong yet compliant microstructures of PVA hydrogels by 3D printing and mechanical training. *(A)* Morphology characterization of 3D-printed freeze-thawed PVA mesh before mechanical training. i and ii are confocal images and corresponding histograms for filaments along both in-plane directions. *P* in the histograms represents the probability of nanofibrils at each aligned direction θ. iii and iv are SAXS patterns in filaments along both in-plane directions. *(B)* Morphology characterization of 3D-printed freeze-thawed PVA mesh after mechanical training. i and ii are confocal images and corresponding histograms for filaments along both in-plane directions. *P* in the histograms represents the probability of nanofibrils at each aligned direction θ. iii and iv are SAXS patterns in filaments along both in-plane directions. *(C)* Images of mechanically-trained mesh with a pre-crack at the stretch of 1.0 and 1.8 under the 1st cycle and the 5000th cycle of loads. *(D)* Effective Young's moduli, *(E)* effective nominal tensile strengths, and *(F)* effective fatigue thresholds of PVA mesh before and after mechanical training. Scale bars are 250 μm *(A)*, *(B)* and 1 cm in *(C)*.